Journal of Computational Physics **160,** 522–540 (2000)
doi:10.1006/jcph.2000.6470, available online at http://www.idealibrary.com on IDEAL®

Unstructured Adaptive Grid Flow Simulations of Inert and Reactive Gas Mixtures

L. F. Figueira da Silva,[1] João L. F. Azevedo,[2] and Heidi Korzenowski[3]

[1]*Laboratoire de Combustion et de Détonique, Centre National de la Recherche Scientifique, 86961 Futuroscope Chasseneuil, France;* [2]*Instituto de Aeronáutica e Espaço, Centro Técnico Aeroespacial, CTA/IAE/ASE-N, 12228-904 São José dos Campos, São Paulo, Brazil; and* [3]*Instituto Tecnológico de Aeronáutica, Centro Técnico Aeroespacial, CTA/ITA/IEA, 12228-900 São José dos Campos, São Paulo, Brazil*
E-mail: da-silva@lcd.ensma.fr, azevedo@iae.cta.br, heidi@aer.ita.cta.br

Received June 1, 1999; revised January 14, 2000

Unstructured adaptive grid flow simulation is applied to the calculation of high-speed compressible flows of inert and reactive gas mixtures. In the present case, the flowfield is simulated using the 2-D Euler equations, which are discretized in a cell-centered finite volume procedure on unstructured triangular meshes. Interface fluxes are calculated by a Liou flux vector splitting scheme which has been adapted to an unstructured grid context by the authors. Physicochemical properties are functions of the local mixture composition, temperature, and pressure, which are computed using the CHEMKIN-II subroutines. Computational results are presented for the case of premixed hydrogen–air supersonic flow over a 2-D wedge. In such a configuration, combustion may be triggered behind the oblique shock wave and transition to an oblique detonation wave is eventually obtained. It is shown that the solution adaptive procedure implemented is able to correctly define the important wave fronts. A parametric analysis of the influence of the adaptation parameters on the computed solution is performed.

Key Words: gas mixtures; reactive flow; unstructured grid methods; finite volume.

1. INTRODUCTION

The use of unstructured grids has received considerable attention in the past few years due to the desire to treat complex flow topologies [1–3]. As flowfields of interest become more complex, it is accepted that only triangular grids in 2-D, or tetrahedral grids in 3-D, possess the degree of flexibility necessary to efficiently discretize the computational domain. In some cases, even if the geometry of the computational domain is simple, complex flowfield configurations can arise due to physical phenomena. Combustion, for instance, may lead to strong heat release together with chemical species transformations in localized regions of

0021-9991/00 $35.00

the flowfield. In the present work an adaptive unstructured grid flow simulation capability is applied to the calculation of high-speed, compressible flows of inert and reactive gas mixtures.

A clear advantage of unstructured grids is that they allow more natural and efficient implementation of solution adaptive refinement procedures, which also are a powerful tool in the simulation of flows with embedded discontinuities. In particular, for reactive flows, different time and length scales are present in the solution and these must be accurately resolved. The characteristic time scale of the slowest chemical reaction may be several orders of magnitude larger than that of the fastest one. Thus, the slowest reaction determines the dimensions of the computational domain and the duration of the computation, while the minimum mesh size required is fixed by the fastest time scale. Moreover, due to the high-activation-energy chemical kinetics associated with the combustion process, fast chemical reactions occur only in a small portion of the space. These considerations naturally lead us to envisage the use of local grid refinement procedures in the present context. Such procedures must be based on adaption strategies that define (i) which regions of the mesh are to be refined; (ii) how the mesh enrichment process is to be performed; (iii) how the information about the new mesh points is to be stored; and (iv) if any post-processing of the new mesh is needed.

The problem of primary interest in the present case is the supersonic flow of a reactive mixture of hydrogen and air over a two-dimensional wedge. Inert and reacting gas flows over this configuration are considered. The onset of combustion downstream of an oblique shock wave stabilized by a wedge has been studied numerically previously by various authors [4–6] using structured mesh solvers. These references show that, even though the geometry of the problem considered is extremely simple, the transition that occurs between the oblique shock wave stabilized by the wedge and the oblique detonation wave involves fairly complex flowfield configurations. In particular, these papers show that heat release due to combustion occurs after an induction length downstream of the leading shock wave. Then, the onset of combustion is responsible for a change on the flow conditions downstream of this initial shock, which leads eventually to the formation of an oblique detonation wave.

In the present case, the flowfield is simulated using the 2-D Euler equations, which are discretized in a cell-centered finite volume procedure on unstructured triangular meshes [7, 8]. Interface fluxes are calculated by a flux vector splitting procedure which guarantees monotone behavior throughout the flowfield [9]. Higher-order spatial accuracy is sought by the use of an extrapolation procedure in which the limited values of the gradients within a cell are used to reconstruct flow properties at the cell interfaces. The adaptation procedure which is used to locally refine the computational mesh consists of three steps. First, the computational cells within which the gradients of some prescribed variables exceed a given threshold are marked. Then, each of the edges of each cell is halved, so that a marked cell is divided into four new ones and its neighbors are divided into either two or four new cells. A smoothing procedure which displaces the cell vertices in order to decrease unwanted cell size variations is then applied.

Flows with variable chemical composition and finite rate chemistry are considered. Physicochemical properties are functions of the local mixture composition, temperature, and pressure, which are computed using the CHEMKIN-II subroutines [10]. A detailed chemical kinetics mechanism for hydrogen–air combustion (9 species, 18 elementary reactions) [11] is used in order to accurately describe all the relevant time scales. The performance of the adaptation procedure is analyzed for both inert and reactive flow computations.

Comparisons are made between structured and unstructured mesh solver results for the oblique shock wave/oblique detonation wave transition problem.

2. THEORETICAL FORMULATION

The 2-D Euler equations for a chemically reacting gas mixture can be written in integral form for a 2-D Cartesian coordinate system [7] as

$$\frac{\partial}{\partial t}\iint_V Q\,dx\,dy + \int_S (E\,dy - F\,dx) = \iint_V \dot{\Omega}\,dx\,dy. \tag{1}$$

Here, V represents the area of the control volume and S is its boundary. The vector of conserved quantities Q is given by

$$Q = [\rho \quad \rho u \quad \rho v \quad \mathcal{E} \quad \rho Y_1 \cdots \rho Y_{J-1}]^T. \tag{2}$$

The expressions for the convective flux vectors, E and F, are

$$E = \begin{Bmatrix} \rho u \\ \rho u^2 + p \\ \rho uv \\ (\mathcal{E} + p)u \\ \rho Y_1 u \\ \vdots \\ \rho Y_{J-1} u \end{Bmatrix}, \qquad F = \begin{Bmatrix} \rho v \\ \rho uv \\ \rho v^2 + p \\ (\mathcal{E} + p)v \\ \rho Y_1 v \\ \vdots \\ \rho Y_{J-1} v \end{Bmatrix}. \tag{3}$$

The chemical source vector can be written as

$$\dot{\Omega} = [0 \quad 0 \quad 0 \quad 0 \quad \dot{\omega}_1 W_1 \cdots \dot{\omega}_{J-1} W_{J-1}]^T. \tag{4}$$

The nomenclature used here is the standard one, such that ρ is the density, u and v are Cartesian velocity components, p is the static pressure, $\mathcal{E}$ is the total energy per unit of volume, and Y_j, $\dot{\omega}_j$, and W_j are the mass fraction, the molar production rate, and the molecular weight of species j, respectively. The mass fraction of species J is calculated by $Y_J = 1 - \sum_{j=1}^{J-1} Y_j$. Equation (1) must be supplemented by the equations of state

$$p = \rho RT \sum_{j=1}^{J} \frac{Y_j}{W_j}, \quad \frac{\mathcal{E}}{\rho} = \sum_{j=1}^{J} Y_j e_j + \frac{1}{2}(u^2 + v^2), \quad \text{where } e_j = h_j^0 + \int_{T_0}^{T} c_{p_j}\,dT - \frac{p}{\rho}. \tag{5}$$

In these equations, T is the static temperature, R is the universal gas constant, and e_j, h_j^0, and c_{p_j} are the internal energy, the standard-state enthalpy, and the specific heat at constant pressure per unit mass of species j, respectively. The specific heat at constant pressure and the standard-state enthalpy for each species are functions of the temperature [10]. The chemical kinetics scheme used involves nine species, H_2, O_2, H_2O, OH, O, H, HO_2, H_2O_2, and N_2, and is due to Balakrishnan and Williams [11]. The use of such a detailed chemical

mechanism is needed to obtain a correct prediction of the different time and length scales present in the reactive flowfields of interest, as well as their variation with the flow conditions [5, 6, 12]. The molar production rates $\dot{\omega}_j$ are given by the Arrhenius law and calculated using the CHEMKIN-II package [10].

3. SPATIAL DISCRETIZATION ALGORITHMS

3.1. First-Order Upwind Scheme

The upwind spatial discretization algorithm implemented in the present work computes interface fluxes using the Liou [9] Advection Upwind Splitting Method (AUSM+). The convective operator, $C(Q_i)$, can be written in the present cell-centered case as

$$C(Q_i) = \sum_{k=1}^{3} (E_{ik}\Delta y_{ik} - F_{ik}\Delta x_{ik}), \tag{6}$$

where $\Delta x_{ik} = x_{k_2} - x_{k_1}$ and $\Delta y_{ik} = y_{k_2} - y_{k_1}$. Figure 1 shows a sketch of a generic triangle layout, including a definition of edge n_1n_2 and associated triangles i and k.

The Liou AUSM+ scheme considers that the convective operator can be expressed as a sum of the convective and pressure terms [9]. The inviscid flux vectors can be written as

$$\begin{aligned} E &= u\Phi + P_x = M_x a\Phi + P_x, \\ F &= v\Phi + P_y = M_y a\Phi + P_y, \end{aligned} \tag{7}$$

where the Φ, P_x, and P_y vectors are defined as

$$\Phi = \begin{Bmatrix} \rho \\ \rho u \\ \rho v \\ \rho H \\ \rho Y_1 \\ \vdots \\ \rho Y_{J-1} \end{Bmatrix} \qquad P_x = \begin{Bmatrix} 0 \\ p \\ 0 \\ 0 \\ 0 \\ \vdots \\ 0 \end{Bmatrix} \qquad P_y = \begin{Bmatrix} 0 \\ 0 \\ p \\ 0 \\ 0 \\ \vdots \\ 0 \end{Bmatrix}. \tag{8}$$

In the previous expressions, H is the total specific enthalpy, $M_x = u/a$, and $M_y = v/a$, where a is the speed of sound.

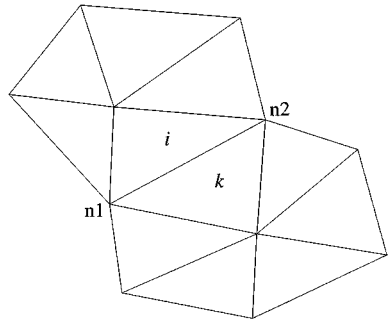

FIG. 1. Sketch of the triangle layout.

The approach followed in the present work in order to extend Liou's ideas [9] to the unstructured grid case consists in defining a local one-dimensional coordinate system normal to the edge considered. The reason for this can be perceived if one observes, based on Eq. (6), that the contribution of the ik edge to the convective operator can be written as [8]

$$\begin{aligned}\text{contrib. of } ik \text{ edge} &= E_{ik}\Delta y_{ik} - F_{ik}\Delta x_{ik} \\ &= \left(E_{ik}n_{x_{ik}} + F_{ik}n_{y_{ik}}\right)\ell_{ik},\end{aligned} \tag{9}$$

where the $\vec{n}_{ik}$ normal to the ik edge, positive outwards with respect to the ith triangle, is defined as

$$\vec{n}_{ik} = n_{x_{ik}}\hat{\imath} + n_{y_{ik}}\hat{\jmath} = \frac{\Delta y_{ik}}{\ell_{ik}}\hat{\imath} - \frac{\Delta x_{ik}}{\ell_{ik}}\hat{\jmath}. \tag{10}$$

Here, ℓ_{ik} is the length of the ik edge. Hence, one can write

$$\text{contribution of } ik \text{ edge} = \left(F_{ik}^{(c)} + P_{ik}\right)\ell_{ik}, \tag{11}$$

where, for now, it is sufficient to write $F_{ik}^{(c)}$ and P_{ik} as

$$\begin{aligned}F_{ik}^{(c)} &= (un_x\Phi + vn_y\Phi)_{ik}, \\ P_{ik} &= (P_x n_x + P_y n_y)_{ik} = p_{ik}\begin{Bmatrix}0\\ n_{x_{ik}}\\ n_{y_{ik}}\\ 0\\ \vdots\\ 0\end{Bmatrix}.\end{aligned} \tag{12}$$

For the construction of the first-order scheme, one must identify the left (or L) state, as defined in Ref. [9], as the properties of the ith triangle and the right (or R) state as those of the kth triangle (see Fig. 1). Hence, the convective operator, as defined in Eq. (6), can finally be written as

$$C(Q_i) = \sum_{k=1}^{3}\left[\left(F_{ik}^{(c)} + P_{ik}\right)\ell_{ik}\right], \tag{13}$$

where

$$F_{ik}^{(c)} = \frac{1}{2}M_{ik}a_{ik}(\Phi_L + \Phi_R) - \frac{1}{2}|M_{ik}|a_{ik}(\Phi_R - \Phi_L), \tag{14}$$

and P_{ik} has already been defined in Eq. (12). The interface Mach number M_{ik} and pressure p_{ik} are defined according to the AUSM+ [9] scheme. Further details of the algorithm implementation can be found in Ref. [8] for the ideal gas case. The second-order scheme follows exactly the same formulation, except that the left and right states are obtained by extrapolation of primitive variables as described in the following section.

3.2. Higher-Order Accuracy

Second-order spatial accuracy is sought in the present case using MUSCL extrapolation [13] of primitive variables (p, u, v, T, Y_j). Such an extrapolation is performed by computing the gradients of the primitive variables within the cell using Green's theorem. The control volume for this integration is chosen to be the computational cell itself. Then, the values of the primitive variables at the cell interfaces are obtained by linear extrapolation from the cell centroids. For the 2-D advection model problem such a procedure is found [14] to be at least as accurate as the one proposed by Barth and Jespersen [15].

In order to avoid oscillations, the extrapolated states must be limited. In the present case, a multidimensional limiter [15] is adopted for all the computations present here. Further details of the limiter construction formulation can be seen in Ref. [14]. However, for some of the different flowfields that have been computed [8], the convergence of the solution, measured in terms of both the L_∞ and the L_2 norms of the residue, seems to stop after two to four orders of magnitude decay. A limiter freezing procedure [16] is implemented in a perfect gas version of this code that led to machine zero convergence on evaluations performed in inert cases. For the reactive cases, one can only reduce the residue by two to three orders of magnitude regardless of the limiter used [7]. A still open question is whether a limiter freezing procedure could improve the convergence of the reactive computations or whether physical reasons prevent achieving machine zero convergence in those cases. It must be emphasized that the inert and reactive flowfields presented here are not subject to further evolution, and they are thus converged in a macroscopic sense.

4. TIME DISCRETIZATION METHODS

The Euler equations, fully discretized in space by an upwind method and assuming a stationary mesh, can be written as

$$\frac{dQ_i}{dt} = -\frac{1}{V_i} C(Q_i) + \dot{\Omega}(Q_i). \tag{15}$$

Time advancement of the solution from time step n to $n+1$ is achieved by the use of Strang's time-step splitting procedure [17]

$$Q_i^{n+1} = \mathcal{L}(\Delta t/2)\mathcal{C}(\Delta t)\mathcal{L}(\Delta t/2) Q_i^n, \tag{16}$$

which separately integrates the fluid dynamics operator $\mathcal{L}$ and the chemistry operator $\mathcal{C}$ at each cell. This procedure is second-order accurate and gives the flexibility of choosing specialized integrators for the chemical kinetics and the fluid dynamics. A more detailed discussion on this subject can be found in the work of LeVeque and Yee [18].

The present work uses a fully explicit, second-order accurate, five-stage Runge–Kutta time-stepping scheme [2] to advance the fluid dynamics part of the governing equations in time. The time integration scheme can therefore be written as

$$\begin{aligned} Q_i^{(0)} &= Q_i^n, \\ Q_i^{(\ell)} &= Q_i^{(0)} - \alpha_\ell \frac{\Delta t_i}{V_i} C\left(Q_i^{(\ell-1)}\right) \qquad \ell = 1, 2, \ldots, 5, \\ Q_i^{n+1} &= Q_i^{(5)}, \end{aligned} \tag{17}$$

where the superscripts n and $n+1$ indicate that these are property values at the beginning and at the end of the nth time step, and the particular values of the α coefficients used are those suggested by Mavriplis [2]. For steady state, inert gas problems, a local time-stepping option has been implemented in order to accelerate convergence [7]. In the reactive flow case, one cannot use a space-varying time step. However, some convergence acceleration can be achieved by recalculating a global time step at each iteration as the minimum of the local Δt_i's obtained from the CFL condition.

The use of a time-step splitting procedure allows the adoption of a specialized solver for the integration of the chemistry operator $\mathcal{C}$ in Eq. (16). This corresponds to a separate integration of the ODE

$$\frac{dQ_i}{dt} = \dot{\Omega}(Q_i). \tag{18}$$

It can be noticed from Eqs. (18) and (1)–(4) that such a time-step splitting procedure results in a constant volume thermal explosion problem in each computational cell. The authors have chosen to perform the integration of Eq. (18) using VODE [19], which is an ODE solver tailored for the solution of problems which include stiff source terms. VODE uses a variable time-step, variable order, backward differentiation algorithm, together with a modified Newton method whose Jacobian matrix is evaluated numerically. This last feature is of particular value when different chemical kinetics schemes are used. A further advantage of using this stiff ODE solver is the fact that it has no stability limits on the choice of the time step. Therefore, only the fluid dynamics requirements constrain the choice of Δt.

5. ADAPTIVE REFINEMENT

The concept behind using an adaptive mesh strategy is to refine regions where large gradients occur. For many problems, the regions that need to be refined are small compared to the size of the computational domain. Therefore, one can reduce storage and CPU requirements by the use of adaptive refinement, when compared with a fixed fine mesh. In order to identify the regions that require grid refinement, a sensor must be defined. The sensor used in this work is based on gradients of flow properties. Its general definition could be expressed as

$$(\text{sensor})_i = \max_m \left(\frac{|\nabla \zeta_m|_i}{\left|\zeta_{m_{\max}} - \zeta_{m_{\min}}\right|} \right); \quad \zeta_m = (p, u, v, T, Y_j), \tag{19}$$

where $\zeta_{m_{\max}}$ and $\zeta_{m_{\min}}$ are the maximum and the minimum values on the whole flowfield and $|\nabla \zeta_m|_i$ is the magnitude of the gradient of the ζ_m property in the ith control volume. As will be seen below, the use of more than one variable to define the sensor is essential to obtain good shock and detonation wave resolution.

5.1. Mesh Enrichment

The first step of the adaptive procedure is to compute the flow on an existing coarse mesh. With this preliminary solution, one can calculate the sensor as previously described. The code marks all triangles in which the sensor exceeds some specified threshold value (the threshold value will be denoted as ι in the present paper), and the marked triangles are refined. A new finer mesh is then constructed by enrichment of the original coarse grid.

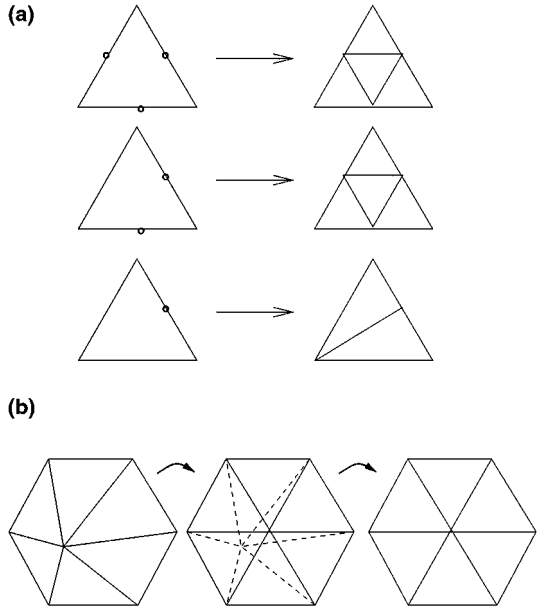

FIG. 2. Schematic representation of (a) the three possible triangle subdivision processes and (b) a single mesh smoothing pass.

The mesh enrichment procedure consists of introducing an additional node for each side of a triangle marked for refinement. For interior sides, this additional node is placed at the mid-point of the side whereas, for boundary sides, it is necessary to refer to the boundary definition to ensure that the new node is placed on the true boundary. After this initial pass, the code has to search all triangles to identify cells that have two or three divided sides. Each of these cells is subdivided into four new triangles. This subdivision may eventually mark new faces. Therefore, this process has to be performed until there are no triangles with more than one marked face. In order to avoid hanging nodes, the triangles that had one marked face should be divided by halving. Figure 2a illustrates the three possible ways of subdividing triangles. In the current implementation of the mesh enrichment procedure, history information about the subdivision process is not stored; i.e., the father triangle identity is given to one of the children. Although this procedure minimizes storage space, it lacks the flexibility which would be desirable in order to introduce mesh coarsening strategies [20]. This feature is certainly a setback if one is to study propagative or unsteady phenomena, which is not the case here, and the issue of mesh coarsening will be addressed in the future.

5.2. Successive Triangle Halvings

The second part of the refinement process consists of identifying all triangles which were refined by halving. This information is stored for the next refinement step because, if there is again an attempt to subdivide these triangles by halving, this is not allowed. The experience has shown [21] that repeated triangle division by halving has a strong detrimental effect in mesh quality. Therefore, if the next refinement step tries to divide by halving a triangle which was obtained by a previous division by halving, the logic in the code forces the

original triangle to be divided into four new triangles before the refinement procedure is allowed to continue. When the mesh enrichment procedure has been completed, the new control volumes receive the property values of their father triangles and the flow solver is re-started.

5.3. Mesh Smoothing

After the mesh enrichment process is achieved, one or more mesh smoothing passes may be performed. The goal of the smoothing process is to smooth out abrupt variations of cell size which, as will be shown below, may occur after several enrichment passes. The smoothing procedure adopted here considers all the triangles that share a common vertex. This vertex is then displaced to the centroid of the polygon formed by the triangles. The unit process is schematically represented in Fig. 2b. It is clear that the mesh connectivity remains unchanged when smoothing is performed. Applying a very large number of smoothing passes would destroy the benefits of the enrichment process. Therefore, an optimum number of smoothing passes exist that preserve the desired decrease of cell size at selected regions of the computational domain, yet allow for a gradual transition from the smallest to the largest meshes. This optimum number of passes is found to be on the order of 5 to 10. It should be noticed that nodes lying at the boundary of the computational domain are not displaced by the smoothing process.

6. RESULTS AND DISCUSSION

6.1. Flowfield Configuration and Initial and Boundary Conditions

The computational procedure described above is applied to the prediction of the supersonic flow of a hydrogen–air mixture around a two-dimensional wedge. The geometry of the computational domain is shown in Fig. 3. The outer boundaries of the domain are either parallel or perpendicular to the wedge surface. The mixture enters the domain from the left and upper boundaries with a given Mach number M, pressure p, temperature T, equivalence ratio and angle of attack δ. The angle of attack is equal to the negative of the wedge half-angle. These conditions are held fixed during the computations presented here. Furthermore, these same values specified as boundary conditions for the left and upper boundaries are used as initial conditions in the whole field to start the calculations. At the wedge surface zero normal temperature gradient ($\partial T/\partial y = 0$) and non-catalytic ($\partial Y_j/\partial y = 0$) and slip

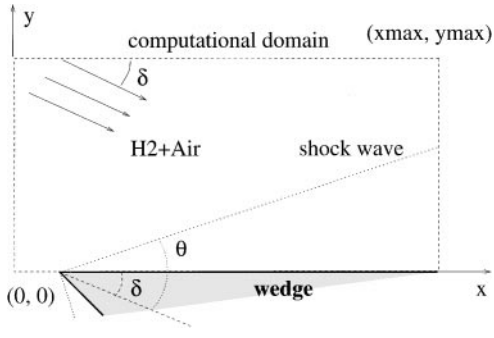

FIG. 3. Schematic representation of the computational domain.

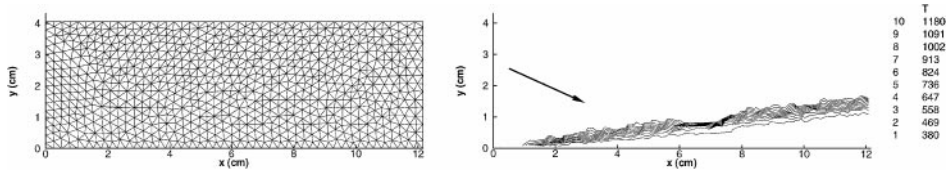

FIG. 4. Initial mesh and temperature (K) field obtained after convergence.

boundary conditions ($\partial u/\partial y = v = 0$) are imposed. At the right (outflow) boundary of the computational domain, characteristic boundary conditions are used [22].

All the computations presented here were performed for the flow of an $M = 8$, $T = 300$ K, $p = 85$ kPa stoichiometric hydrogen–air mixture around a wedge with a half-angle of 23.8°. The initial mesh used contains 1504 triangles and 816 nodes, as shown in Fig. 4. The computational domain spans over $(x, y) = (0:12, 0:4)$ cm.

Such flow and boundary conditions, which lead to stable oblique shock waves for inert gases, may give rise to a complex flow topology in the presence of combustion. As will be seen in the forthcoming sections, when ignition of the reactive mixture occurs downstream of the leading oblique shock wave, an oblique shock wave/oblique detonation wave transition is observed.

6.2. Inert Flow

Before we present the results in which chemistry is taken into account, it is useful to examine the calculations performed for an inert gas flow. The results in Fig. 4, where the initial mesh and the temperature contours obtained after convergence are plotted, show that the shock wave is resolved within three computational cells. Due to the coarseness of this mesh, the actual thickness of the oblique shock wave is comparable to the dimensions of the computational domain. In order to obtain a smaller ratio of shock thickness to domain dimension, three passes of adaptive refinement are performed. In this case, a sensor based on the gradients of the primitive variables (p, u, v, T) is used. The value of the threshold is $\iota = (0.1, 0.1, 0.05)$ for each refinement pass. Convergence of the result on each mesh is achieved before mesh refinement. The final refined mesh contains 7630 triangles and 3908 nodes. Figure 5 shows the mesh and the temperature field for the converged solution in the final refined mesh. In this case, smoothing of the mesh after each mesh enrichment pass is not active. It can be seen in Fig. 5 that mesh refinement leads to a dramatic reduction of the thickness of the numerical shock wave. It should be noticed, though, that the number of computational cells across the shock remains unchanged when the mesh is refined.

Figure 6 shows the final adapted mesh and the temperature contours when three mesh enrichment passes are performed, after each of which 10 smoothing passes were made. All

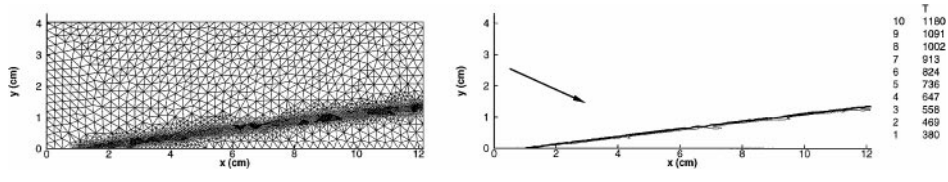

FIG. 5. Adapted mesh and the corresponding temperature (K) contours with no mesh smoothing, adaptation on (p, u, v, T), $\iota = (0.1, 0.1, 0.05)$.

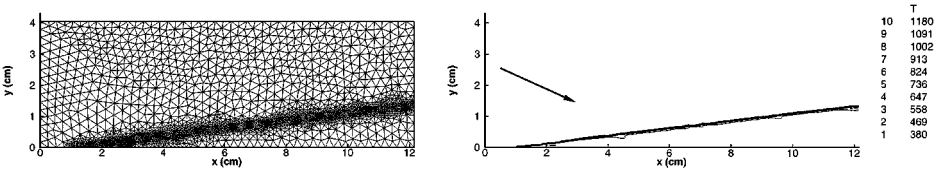

FIG. 6. Adapted mesh and the corresponding temperature (K) contours with 10 smoothing passes after each mesh enrichment pass, adaptation on (p, u, v, T), $\iota = (0.1, 0.1, 0.05)$.

the other flow and solver parameters used are the same as above. The numbers of nodes and volumes in this resulting mesh are 3969 and 7748, respectively. Even though the quality of the solution is not affected by the smoothing procedure, the spatial distribution of cell sizes varies more gradually, when compared to the results shown in Fig. 5. A distinctive feature of this smoothed mesh is the secondary mesh clustering that occurs by spots. As shown in Fig. 7, those spots are found to lie near the boundary of a mesh enriched region. Indeed, the nodes in these regions have more connections toward one preferential direction. Thus, the mesh smoothing procedure displaces a given node toward this direction, leading to the observed clustering.

The history of the L_2 norm of the residual, corresponding to the results in Figs. 5 and 6, is shown in Fig. 8. A sudden increase of these norms is observed each time the mesh is adapted. Then, the residuals gradually decrease, eventually reaching a constant value. A frozen limiter procedure [16], not implemented in this version of the computer code, leads to machine zero convergence for ideal gas calculations under similar flow conditions. It should be noticed that the convergence process is stalled sooner when the mesh is not smoothed. This is found to be a direct consequence of the secondary clustering of mesh points: a reduction in the minimum cell size is observed when smoothing is performed. Indeed, the ratio of minimum characteristic mesh sizes (defined by the radius of the inscribed circle) for the non-smoothed and the smoothed meshes is 2.9 : 1. In the present constant time-step computations, the benefits of mesh smoothing seem to be counterbalanced by this minimum cell size decrease. This is not the case when the variable time-step option is used.

6.3. Reacting Flow

The supersonic flow of a reactive mixture over 2-D wedges has been studied both numerically [4–6, 12] and experimentally [5, 23, 24] in the past few years. In these cases, delayed transitions from oblique shock waves (OSW) to oblique detonation waves (ODW) were obtained which involve strong couplings between compressibility and high activation

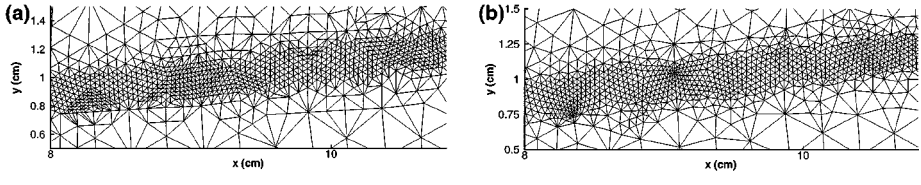

FIG. 7. Adapted mesh corresponding to (a) no smoothing and (b) 10 smoothing passes after each mesh enrichment pass; enlarged view of Figs. 5 and 6.

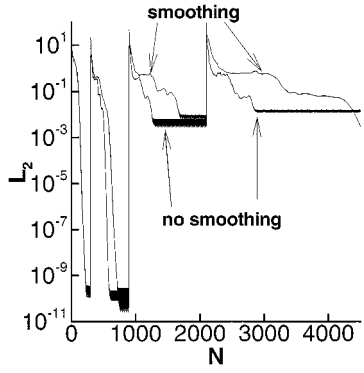

FIG. 8. Logarithm of the L_2 norm of the residual, inert flows.

energy, exothermic, chemical kinetics. A typical example of such a transition is shown in Fig. 9, in which the fields of H_2O and OH mass fraction, pressure and temperature are plotted for the same flow and geometrical conditions used for the inert computations. These results are obtained using a second-order, upwind structured mesh solver based on the same flux splitting method [5, 6, 12] on a uniform Cartesian grid containing 200×120 points. The results presented in Fig. 9 are considered a baseline calculation for comparison with the unstructured mesh computations, since the mesh spacing is of the order of the minimum cell size obtained after two refinement passes, starting from the mesh shown in Fig. 4.

The computational results presented in Fig. 9 show that, when wedge-stabilized OSW/ODW transition occurs, the resulting flowfield may be divided into three regions [4–6, 12]:

1. An *induction region*, where an OSW whose angle is identical to the one obtained in the inert case exists. The thermodynamic conditions prevailing in this region are fixed by the jump conditions across the leading OSW. Chain initiation and chain branching reactions dominate the chemical process, with negligible heat release.

2. A *transition region*, where the sudden onset of chain termination reactions leads to an increase of the flow temperature at the vicinity of the wedge surface. Pressure waves, which are fed by this temperature increase, propagate towards the leading OSW, modifying the flow conditions downstream of this shock wave. A decrease of the chemical induction time results, which, associated with the coalescence of pressure waves, is responsible for the

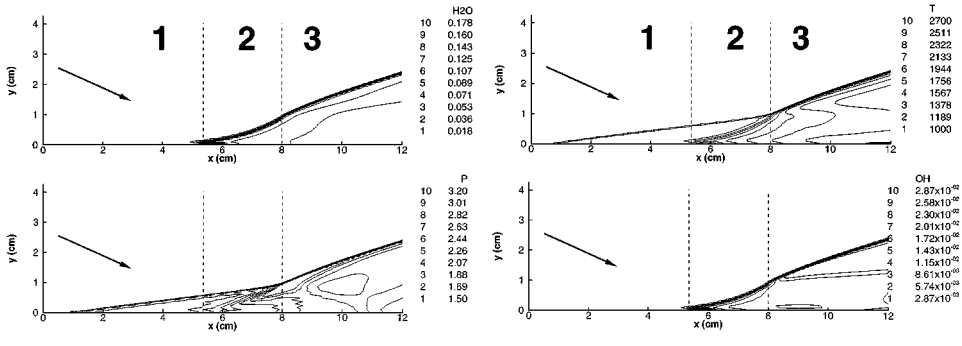

FIG. 9. Fields of temperature (K), pressure (atm), and OH and H_2O mass fractions for a baseline structured mesh computation.

formation of a detonation wave in the shocked gas region. This detonation wave intercepts the initial OSW in a triple point from which a slip line and an expansion fan emanate.

3. A *detonation region*, where the initial ODW that was formed in the transition region relaxes towards the strong overdriven detonation corresponding to this given wedge angle and flow conditions. Such a relaxation is due to the interaction between the ODW and the wedge-reflected expansion fan. The slip line that originates at the triple point separates gases that have crossed the final ODW only from the burned mixture that crossed both the leading OSW and the transition region.

In this context, one of the major motivations for the work described here is to implement an adaptive refinement capability which would allow further focusing on the regions of interest without an excessive increase in the computational cost. This adaptive refinement capability, embedded in the overall unstructured grid approach, should allow the creation of new control volumes only in relevant portions of the flow and, therefore, a higher level of refinement and understanding of the physical phenomena in the transition and detonation regions. The present paper, however, does not attempt to exploit yet the capability in order to improve the understanding of the physical process, but is mostly concerned with the validation and test of the proposed unstructured grid capability for high speed combustion applications.

The adaptive refinement procedure described in the previous sections is influenced by: (i) the choice of the variables which will be used to define the sensor; (ii) whether smoothing is allowed or not; (iii) the threshold ι. Moreover, the number of refinement passes is a crucial parameter, since the accuracy of the computed results depends on the mesh size. The influence of these parameters on the computed solution is examined now.

6.3.1. *Influence of the Choice of the Sensor Variables*

Depending on the choice of the variables used as sensors in Eq. (19), the mesh enrichment procedure halves the triangle edges in different regions of the flowfield. In Figs. 10–12 the final adapted mesh, the pressure, the temperature, and the OH mass fraction are plotted when (p, u, v, T), (p, u, v, T, Y_j), and $(\rho, \rho u, \rho v, \mathcal{E}, \rho Y_j)$ are used as sensors, respectively. Three adaptive refinement passes are made, with $\iota = (0.2, 0.1, 0.05)$, each followed by 10 smoothing passes. The final numbers of volumes and nodes are (7,154 and 3,665), (9,834 and 5,019), and (10,475 and 5,346), respectively.

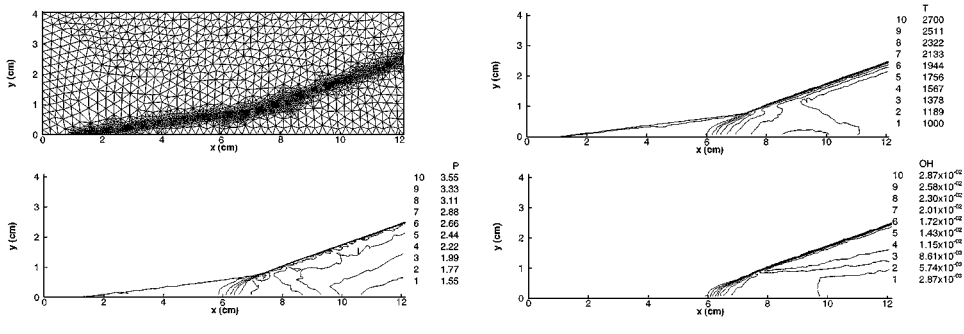

FIG. 10. Final adapted mesh, temperature (K), pressure (atm), and OH mass fraction field for adaptation on (p, u, v, T), $\iota = (0.2, 0.1, 0.05)$, with mesh smoothing.

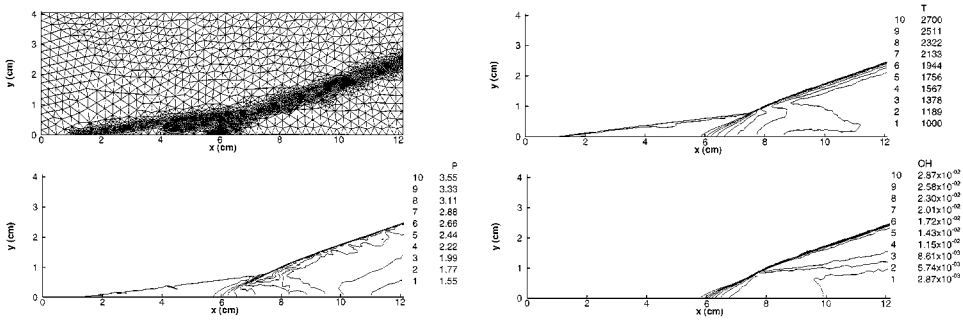

FIG. 11. Final adapted mesh, temperature (K), pressure (atm), and OH mass fraction field for adaptation on (p, u, v, T, Y_j), $\iota = (0.2, 0.1, 0.05)$, with mesh smoothing.

The comparison of these figures shows that the overall features of the flowfield, i.e., the induction length, the transition region, and the ODW angle, are in good agreement with the results of the baseline structured code shown in Fig. 9. On the other hand, the result obtained when the sensor variables are (p, u, v, T) has a lack of mesh resolution in the transition region. The transition region is found to be correctly resolved both when the primitive (p, u, v, T, Y_j) and when the conserved $(\rho, \rho u, \rho v, \mathcal{E}, \rho Y_j)$ variables are used, the former leading to a smaller number of nodes and volumes. The use of the mass fractions Y_j only as sensors was not attempted, since this would lead to a coarse mesh for the leading OSW, which is clearly an undesirable feature. These results clearly show that adaption based on the mass fractions Y_j is essential to the rendering of the OSW/ODW transition. This is due to the fact that, within the transition region, the chemical process involves $O(1)$ changes in the mass fractions with only moderate variations in p, u, v, T.

It can also be seen in Figs. 10–12 that the enrichment process does not refine the mesh around the slip line which emanates from the triple point. Indeed, as it is shown below, a smaller value of the ι parameter is needed, since the gradients there are much smaller than those across both the OSW and the ODW.

6.3.2. *Influence of the Mesh Smoothing*

In Fig. 13, the final adapted mesh, the temperature and OH mass fraction fields obtained using the primitive variables (p, u, v, T, Y_j) as sensors and $\iota = (0.2, 0.1, 0.05)$ are plotted.

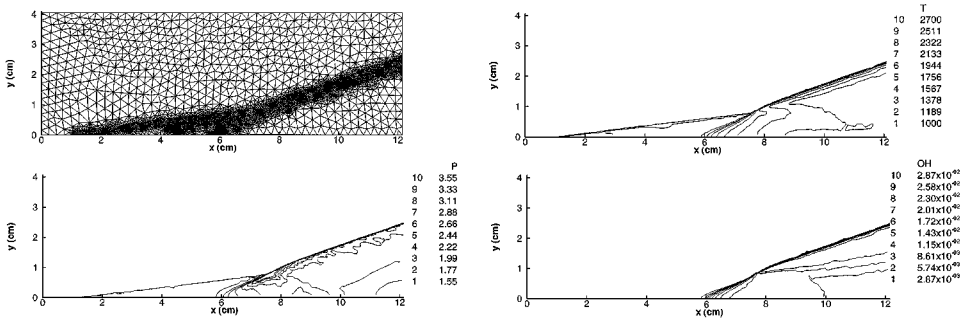

FIG. 12. Final adapted mesh, temperature (K), pressure (atm), and OH mass fraction field for adaptation on $(\rho, \rho u, \rho v, \mathcal{E}, \rho Y_j)$, $\iota = (0.2, 0.1, 0.05)$, with mesh smoothing.

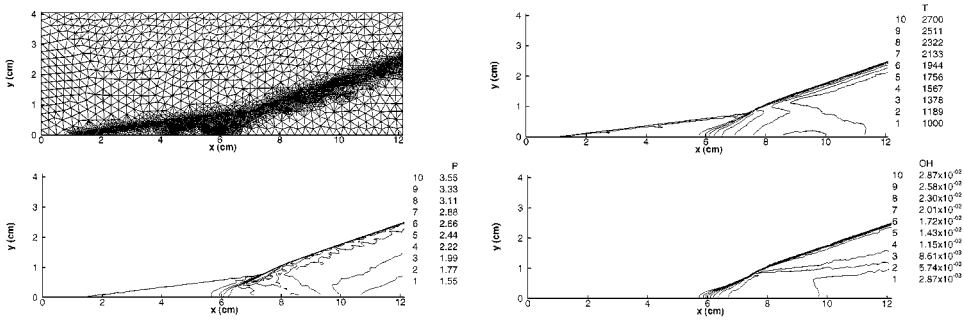

FIG. 13. Final adapted mesh, temperature (K), pressure (atm), and OH mass fraction field for adaptation on (p, u, v, T, Y_j), $\iota = (0.2, 0.1, 0.05)$, no mesh smoothing.

No smoothing passes are performed. The final mesh contains 11,168 triangles and 5692 nodes. The results shown in this figure were obtained using exactly the same flow and solver parameters except for the smoothing passes, as those presented in Fig. 11. Thus, when smoothing is not performed, the final mesh is found to have 15% more nodes. This tendency, although contradictory to the one observed for the inert cases, has been observed in all the reactive flow computations that have been performed by the authors. These figures show good agreement between the results computed with and without smoothing. The benefits of smoothing on the quality of the solution are only evidenced at the end of the transition region and the vicinity of the wall $[(x, y) = (7, 0)]$, where the contour plots are slightly jagged for the unsmoothed case.

As already noticed in the inert computations, smoothing of the mesh leads to a decrease in the minimum triangle size, which in the present case is 0.56 mm without smoothing and 0.30 mm for the final smoothed mesh. The corresponding time steps are also on the same 0.54 ratio. Thus, as can be verified in the L_2 residual plots of Fig. 14, the convergence of the non-smoothed mesh is almost two times faster than that of the smoothed mesh. Therefore, the forthcoming comparisons do not include smoothing of the computational mesh.

Convergence of the reactive flow simulations also seems to stall after a few orders of magnitude decay in the residue, regardless of whether mesh smoothing is used or not. As discussed in Section 6.2, the use of limiter freezing procedures may lead to machine zero convergence. Furthermore, previous experience with the structured mesh calculations [6, 12]

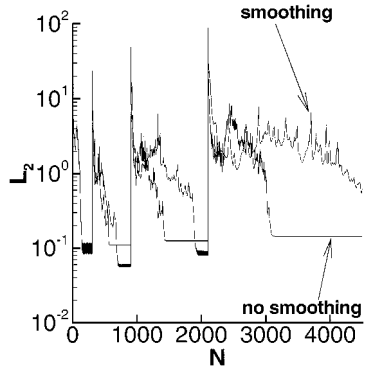

FIG. 14. Logarithm of the L_2 norm of the residual, reactive flows.

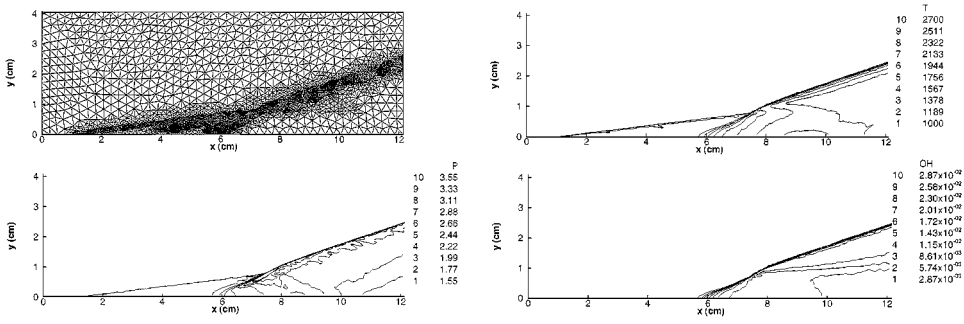

FIG. 15. Final adapted mesh, temperature (K), pressure (atm), and OH mass fraction field for adaptation on (p, u, v, T, Y_j), $\iota = (0.1, 0.1, 0.05)$, no mesh smoothing.

has presented similar behavior as far as the convergence of the residual for reactive flow simulations is concerned. It must be noticed, though, that as meshes become increasingly fine, the detailed reactive flow result should capture the inner structure of detonation waves, which include unsteady transverse and longitudinal waves. The onset of these waves could be responsible for the L_2 norm of the residual not reaching machine zero.

6.3.3. *Influence of the Threshold* ι

In order to evidence the influence of the threshold ι, Figs. 15 and 16 present the results of the computations performed when the value of the threshold is halved either at the first or at the last adaption [$\iota = (0.1, 0.1, 0.05), (0.2, 0.1, 0.025)$], respectively. All the other flow and mesh adaption parameters are the same as those of Fig. 13. The final numbers of volumes and nodes are (11,524 and 5,872) and (12,062 and 6,144), respectively. As expected, decreasing the value of the threshold increases the number of added nodes. Both cases show an improvement in the number of volumes at the burned gases region, leading to a better mesh resolution around the slip line.

A detailed comparison of the final adapted mesh plotted in Figs. 13, 15, and 16 shows that the spatial extent of the triangles added by the adaption process is larger when the threshold ι is reduced at early stages of the computation. Thus, decreasing the value of the threshold at the later stages of the adaption procedure is a more effective way of distributing the mesh points. This is due to the fact that the new volumes are smaller than those added during the

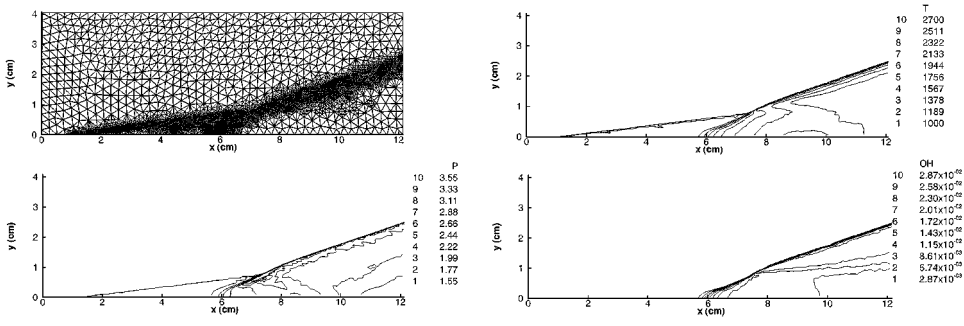

FIG. 16. Final adapted mesh, temperature (K), pressure (atm), and OH mass fraction field for adaptation on (p, u, v, T, Y_j), $\iota = (0.2, 0.1, 0.025)$, no mesh smoothing.

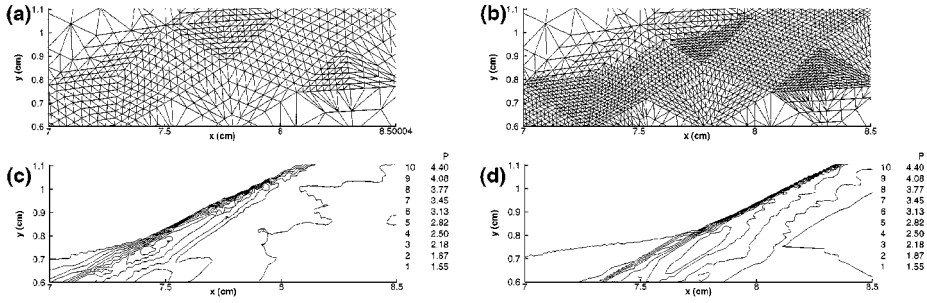

FIG. 17. Final adapted mesh and pressure fields (atm) after three (a and c) and four (b and d) adaptation passes, adaptation on (p, u, v, T, Y_j), $\iota = (0.2, 0.1, 0.025, 0.01)$, no mesh smoothing.

initial stages of adaption and thus have a greater contribution to the spatial resolution of the physical phenomena. This is of particular interest in the present OSW/ODW computation, where the spatial extent of the shock waves is decreased with successive refinements.

6.3.4. *Influence of the Number of Adaption Passes*

Departing from the results shown in Fig. 16, a fourth adaptation pass is performed using $\iota = 0.01$. The final mesh contains 37,168 triangles and 18,744 volumes. This supplementary mesh adaption pass is unnecessary, as far as the overall flow structure is concerned. However, some of the details of the computed solution are subject to change. For instance, this can be verified in Fig. 17, where enlargements of the mesh and the pressure field in the transition region are plotted. These results are obtained once steady state is achieved after three and four adaption passes. This is further illustrated in Fig. 18, where the evolution of temperature, pressure, and mass fractions of OH and H across the oblique detonation wave is plotted. This figure shows that the finer mesh brings no change either in the final values of these variables or in the peak values of T and Y_{OH}. On the other hand, the peak value of H mass fraction and p increase nearly 13 and 6%, respectively. A similar trend is also observed

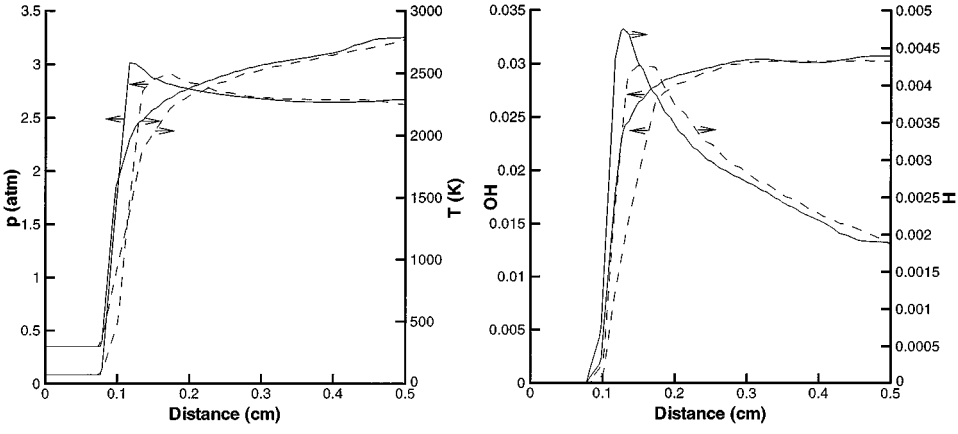

FIG. 18. Temperature (K), pressure (atm), and OH and H mass fraction evolution as a function of the distance normal to the ODW. Starting point $(x, y) = (11.02, 2.17)$; results after (- - -) three and (—) four mesh adaptation passes.

for HO_2 and H_2O_2 radicals. An expected effect of the finer mesh is the observed sharper shock capture. It should be noticed that the characteristic cell size corresponding to the finest mesh, which is on the order of 0.3 mm, is still too large to capture details of the inner structure of the detonation wave. Further refinement is not deemed practical at this point, since the CPU time to convergence on this last mesh is on the order of 20 days on a HP PA-7200 120-MHz processor. Three approaches to reducing this prohibitive execution time should be envisaged: (i) processor architecture oriented optimization, such as improving data locality on the cache; (ii) mesh coarsening, with the additional benefit of decreasing storage requirements; and (iii) code parallelization.

7. CONCLUDING REMARKS

Computational results were presented for the case of premixed hydrogen–air flow over a 2-D wedge. In this case, combustion may be triggered behind the oblique shock wave and transition to an oblique detonation wave is eventually obtained. Attention was focused on sharp resolution of both the shock and detonation waves. Comparisons were made with independent calculations and good agreement was observed for the range of parameters investigated. Although the use of unstructured adaptive meshes is commonplace in aerodynamic applications today, the same is not true for combustion in supersonic flows. The unstructured adaptive solution procedure implemented was able to correctly define the important wave fronts while still offering a computationally efficient option for complex flow topologies. Moreover, the results also verify that the capability of using solution adaptive meshes has provided a far better resolution of such waves than previous calculations by Azevedo and Figueira da Silva [7]. Mesh adaption based on fluid and chemistry variables was found to be essential to the correct prediction of OSW/ODW transitions. From a physical point of view, however, additional mesh adaption passes would be desirable to achieve a detonation wave which is resolved to the smallest spatial scales. This will be the subject of future work together with improved mesh smoothing after refinement.

ACKNOWLEDGMENTS

This work was accomplished in the framework of an international cooperation agreement between Conselho Nacional de Desenvolvimento Científico e Tecnológico (CNPq) and Centre National de la Recherche Scientifique (CNRS). The authors gratefully acknowledge the additional partial support of CNPq through a doctoral scholarship for the third author (Process 141156/94-5) and under Integrated Project Research Grant 522413/96-0. Financial support from the Casimiro Montenegro Filho Foundation during the first author's sojourn at ITA is also gratefully acknowledged.

REFERENCES

1. A. Jameson and D. Mavriplis, Finite volume solution of the two-dimensional Euler equations on a regular triangular mesh, *AIAA J.* **24**(4), 611 (1986).
2. D. J. Mavriplis, Multigrid solution of the two-dimensional Euler equations on unstructured triangular meshes, *AIAA J.* **26**(7), 824 (1988).
3. V. Venkatakrishnan, Perspective on unstructured grid flow solvers, *AIAA J.* **34**(3), 533 (1996).
4. C. Li, K. Kailasanath, and E. Oran, Detonation structures behind oblique shocks, *Phys. Fluids* **6**(4), 1600 (1994).

5. C. Viguier, L. F. Figueira da Silva, D. Desbordes, and B. Deshaies, Onset of oblique detonation over a wedge: Comparison between experimental and numerical results, in *Twenty-Sixth Symposium (International) on Combustion* (The Combustion Institute, Pittsburgh, 1996), p. 3023.
6. B. Deshaies, L. F. Figueira da Silva, and M. René-Corail, Some generic problems related to combustion of hydrogen and air in supersonic flows, in *IUTAM Symposium on Combustion in Supersonic Flows*, edited by M. Champion and B. Deshaies (Kluwer, Dordrecht/Norwell, MA, 1997), pp. 15–42.
7. J. L. F. Azevedo and L. F. Figueira da Silva, The development of an unstructured grid solver for reactive compressible flow applications, in *33rd AIAA/ASME/SAE/ASEE Joint Propulsion Conference and Exhibit*, American Institute of Aeronautics and Astronautics, Seattle, WA, July 1997 (unpublished).
8. J. L. F. Azevedo and H. Korzenowski, Comparison of unstructured grid finite volume methods for cold gas hypersonic flow simulations, in *16th AIAA Applied Aerodynamics Conference*, American Institute of Aeronautics and Astronautics, Albuquerque, NM, June 1998, pp. 447–463.
9. M.-S. Liou, A sequel to AUSM: AUSM+, *J. Comput. Phys.* **129**, 364 (1996).
10. R. J. Kee, F. M. Rupley, and J. A. Miller, CHEMKIN-II: A Fortran Chemical Kinetics Package for the Analysis of Gas Phase Chemical Kinetics, SAND89-8009B/UC-706, Sandia National Laboratories, Nov. 1991.
11. G. Balakrishnan and F. A. Williams, Turbulent combustion regimes for hypersonic propulsion employing hydrogen–air diffusion flames *J. Propuls. Power* **10**(3), 434 (1994).
12. L. F. Figueira da Silva, and B. Deshaies, Stabilization of an oblique detonation wave by a wedge: A parametric numerical study, *Combust. Flame* **121**(1–2), 152 (2000).
13. B. van Leer, Flux-Vector Splitting for the Euler Equations, in *Proc. of the 8th International Conference on Numerical Methods in Fluid Dynamics*, edited by E. Krause, Lect. Notes in Phys. (Springer–Verlag, Berlin, 1982), Vol. 170, pp. 507–512.
14. J. L. F. Azevedo, L. F. Figueira da Silva, and D. Strauss, Order of accuracy analysis for unstructured grid finite volume upwind schemes, submitted for publication.
15. T. J. Barth and D. C. Jespersen, The design and application of upwind schemes on unstructured meshes, in *27th AIAA Aerospace Sciences Meeting*, American Institute of Aeronautics and Astronautics, Reno, NV, Jan. 1989 (unpublished).
16. V. Venkatakrishnan, Convergence to steady state solutions of the Euler equations on unstructured grids with limitiers, *J. Comput. Phys.* **118**, 120 (1995).
17. G. Strang, On the construction and comparison of difference schemes, *SIAM J. Numer. Anal.* **5**, 506 (1968).
18. R. J. LeVeque and H. C. Yee, A study of numerical methods for hyperbolic conservation laws with stiff source terms, *J. Comput. Phys.* **86**(1), 187 (1990).
19. G. D. Byrne and A. M. Dean, The numerical solution of some kinetics models with VODE and CHEMKIN II, *Comput. Chem.* **17**(3), 297 (1993).
20. A. Povitsky and D. Ofengeim, *Numerical Study of Interaction of a Vortical Density Inhomogeneity with Shock and Expansion Waves*, NASA/CR-1998-206918, National Aeronautics and Space Administration; also ICASE Report No. 98-10, Institute for Computer Applications in Science and Engineering, Feb. 1998.
21. H. Korzenowski, *Unstructured Mesh Techniques for the Simulation of High Mach Number Flows* (in Portuguese), Ph.D. thesis, Instituto Tecnológico de Aeronáutica, São José dos Campos, June 1998.
22. K. W. Thompson, Time dependent boundary conditions for hyperbolic systems, *J. Comput. Phys.* **68**, 1 (1987).
23. E. K. Dabora, D. Desbordes, C. Guerraud, and H. G. Wagner, Oblique detonation at hypersonic velocities, in *Dynamics of Detonations and Explosions: Detonations*, edited by A. L. Kuhl, A. A. Borisov, J.-C. Leyer, and W. A. Sirignano, Progress in Astronautics and Aeronautics (American Institute of Aeronautics and Astronautics, Washington, D.C., 1991), Vol. 133, p. 187.
24. J. C. Liu, J. J. Liou, M. Sichel, C. W. Kaufmann, and J. A. Nichols, Diffraction and transmission of a detonation into a bounding explosive layer in *Twenty-Sixth Symposium (International) on Combustion* (The Combustion Institute, Pittsburgh, 1987), p. 1639.